

# Positive and negative magnetoresistance phenomena observed in magnetic electrospun polyacrylonitrile-based carbon nanocomposite fibers

Cite this: *J. Mater. Chem. C*, 2014, 2, 715

Jiahua Zhu,<sup>ab</sup> Minjiao Chen,<sup>ac</sup> Honglin Qu,<sup>ac</sup> Huige Wei,<sup>ac</sup> Jiang Guo,<sup>ac</sup> Zhiping Luo,<sup>d</sup> Neel Haldolaarachchige,<sup>e</sup> David P. Young,<sup>e</sup> Suying Wei<sup>\*ac</sup> and Zhanhu Guo<sup>\*a</sup>

Unique temperature dependent resistance behavior (positive/negative temperature coefficient switching at 240 K), and tunable negative and positive magnetoresistance switching phenomena were observed in the magnetic carbon nanocomposite fibers prepared from heat treatment of the nitrate soaked oxidation stabilized polyacrylonitrile (PAN) nanofibers. The physical mechanisms were revealed by considering the variable range hopping electron transportation model, electron quantum interference and spin-dependent scattering effects.

Received 10th October 2013  
Accepted 6th November 2013

DOI: 10.1039/c3tc32007c

www.rsc.org/MaterialsC

## 1. Introduction

Giant magnetoresistance (GMR), first discovered in alternating ferromagnetic iron and non-ferromagnetic chromium layers in 1988,<sup>1</sup> is defined as a large change in resistance when the relative orientation of the magnetic domains (magnetization) in adjacent layers is adjusted from anti-parallel to parallel under an applied magnetic field. During the last two decades, GMR has been discovered in various material systems, such as carbon (carbon nanotubes<sup>2</sup> and graphene<sup>3–5</sup>), polymers,<sup>6,7</sup> conductive polymers as well as their nanocomposites.<sup>8–12</sup> Among them, carbon nanocomposites have attracted much interest in recent years due to their tunable GMR properties by integrating functional nanostructures.<sup>13,14</sup> Besides, carbon morphology control seems another effective approach to achieve a desired GMR behavior.<sup>15,16</sup>

Fibrous nanocomposites by assembling different nanostructures into a one-dimensional fibrous structure possess unique physicochemical properties that are essentially different from those of the components taken separately. These unique properties have been utilized to upgrade the current techniques

in different emerging areas including catalysis, sensing, energy storage, environmental remediation, *etc.* For example, Pt–Ru/carbon fiber nanocomposites have been utilized as anode catalysts for direct methanol fuel cells,<sup>17</sup> Pt(Pd)/TiO<sub>2</sub> nanocomposite fibers were produced as effective catalysts for organic dye degradation and H<sub>2</sub> generation.<sup>18</sup> Some other nanocomposite fibers with unique structures achieve superior performance in electrochemical energy storage,<sup>19,20</sup> hydrogen storage,<sup>21</sup> chemical sensors,<sup>22–24</sup> and biosensors.<sup>25,26</sup> Until now, little work has been done in this area to reveal the magnetoresistive behavior of fibrous carbon nanocomposites decorated with different nanostructures. A better understanding of the magnetoresistance phenomenon of these fibrous carbon nanocomposites will definitely trigger their wide applications in the field of computer memory and storage technology, biosensing and biochips, spin-electronics and magnetoelectronics.

Recently, electrospinning technology has received great attention due to its low manufacturing cost and high production for fabricating polymeric micro- and nano-fibers on a large scale as compared to other technologies, such as melt fibrillation,<sup>27</sup> nanolithography,<sup>28</sup> and self-assembly.<sup>29,30</sup> This facile technology has also been explored to manufacture nanocomposite fibers with an aim to incorporate unique physical, chemical and biological properties into the polymer fibers. As a result, nanocomposite fibers with enhanced mechanical and thermal properties have been reported in polymer blends and inorganic–organic hybrid nanofibers.<sup>31–34</sup> To achieve the desired functionality, uniform distribution of functional nanostructures within the fiber substrate is critically important. Two major approaches have been developed to manufacture nanocomposite fibers using the electrospinning technique. First,

<sup>a</sup>Integrated Composites Laboratory (ICL), Dan F Smith Department of Chemical Engineering, Lamar University, Beaumont, TX 77710, USA. E-mail: zhanhu.guo@lamar.edu; Tel: +1 (409)880-7654

<sup>b</sup>Chemical and Biomolecular Engineering, The University of Akron, Akron, OH 44325, USA

<sup>c</sup>Department of Chemistry and Biochemistry, Lamar University, Beaumont, TX 77710, USA. E-mail: suying.wei@lamar.edu; Tel: +1 (409)880-7976

<sup>d</sup>Department of Chemistry and Physics, Fayetteville State University, Fayetteville, NC 28301, USA

<sup>e</sup>Department of Physics and Astronomy, Louisiana State University, Baton Rouge, LA 70803, USA

physical blending of nanostructures and polymer solution or melts into a mixture before spinning has been reported.<sup>35–37</sup> However, this approach often leads to a serious agglomeration of the nanoscale additives due to the incompatibility between the hydrophobic polymer and hydrophilic inorganic nanostructures, resulting in discontinuity and unintended or defective functionalities in the fibers. And also, gravity separation of the heavier component is another issue that brings nonuniformity in the resulting nanocomposite fibers unless a stabilized homogeneous mixture could be obtained. Second, blending of the nanomaterial precursor and polymer solution into a homogeneous mixture and processing into fibers have been reported using the electrospinning technique. And then the nanostructures are grown *in situ* via a post chemical/thermal treatment process. The second approach is more favorable in terms of better control on nanostructure size and dispersion quality. However, this method also has its limitations in complex nanostructure precursor preparation, selection of solvent that should be able to dissolve the precursor and polymer simultaneously, viscosity control, *etc.* Therefore, the utilization of a simple and cost-effective method to prepare nanocomposite fibers is important and in urgent demand in the nanoscience and nanotechnology field.

In this work, a facile dip coating approach has been reported to either coat metal oxide nanostructures on a carbon fiber surface or to embed nanostructures within the carbon fiber body. Unique positive/negative temperature coefficient switching phenomena and positive/negative magnetoresistance have been observed in the manufactured fibrous carbon nanocomposites coated by different metal oxide nanostructures. The microstructure, temperature dependent electrical resistance, and magnetic properties of the fiber nanocomposites are carefully studied and their electron transportation mechanisms have been revealed as well.

## 2. Experimental section and characterization

### 2.1 Materials

Polyacrylonitrile (PAN,  $M_w = 150\,000$ ,  $X_n = 283$  and the density is  $1.184\text{ g cm}^{-3}$ ) was purchased from Scientific Polymer Products Inc. Anhydrous *N,N*-dimethylformamide (DMF, 99.9%), iron nitrate nonahydrate ( $\text{Fe}(\text{NO}_3)_3 \cdot 9\text{H}_2\text{O}$ , >98.0%), and cobalt nitrate hexahydrate ( $\text{Co}(\text{NO}_3)_2 \cdot 6\text{H}_2\text{O}$ , >97.7.0%) were purchased from Alfa Aesar company. All these materials were used as-received without any further treatment.

### 2.2 Preparation of pure PAN fibers

The PAN–DMF solutions were prepared by magnetic stirring at  $60.0\text{ }^\circ\text{C}$  for half an hour with a polymer loading of 10.0 wt%. Pure PAN fibers were prepared using an electrospinning method.<sup>35</sup> Typically, a 10 mL syringe with a stainless steel gauge needle (inner diameter, 0.70 mm) was used to load the polymer solution. A high-voltage power supply (Gamma High Voltage Research, Product HV Power Supply, Model no. ES3UP-5w/DAM) was used and connected to the stainless needle. The grounded counter electrode was a flat aluminum foil. The polymer solution was constantly and continuously supplied by a syringe pump (NE-300, New Era Pump System, Inc.). The applied voltage, volume feed rate and tip-to-collector distance were 20.0 kV,  $20.0\text{ }\mu\text{L min}^{-1}$  and 20.0 cm, respectively.

### 2.3 Preparation of magnetic carbon-composite fibers (MF)

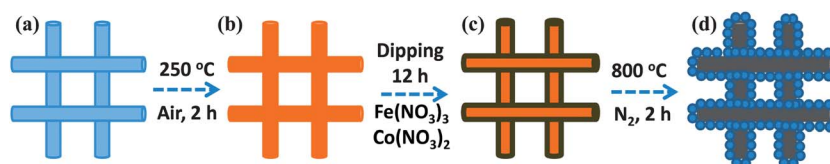
The preparation of MFs took place in three steps as illustrated in Scheme 1: (1) thermal stabilization of PAN fibers at  $250\text{ }^\circ\text{C}$  for 2 hours in air atmosphere with a heating rate of  $2\text{ }^\circ\text{C min}^{-1}$ ; (2) dipping the stabilized PAN fibers in different inorganic salt solutions for 12 hours and then drying the fibers at  $80\text{ }^\circ\text{C}$ ; (3) carbonization at  $800\text{ }^\circ\text{C}$  for 2 hours in nitrogen with a heating rate of  $5\text{ }^\circ\text{C min}^{-1}$ ; (4) nanoparticle oxidation at  $250\text{ }^\circ\text{C}$  for 2 hours in air with a heating rate of  $5\text{ }^\circ\text{C min}^{-1}$  and then cooling down naturally. The carbon fibers produced from different heat treatments are designated as CF, MF1, and MF2. CF represents carbon fibers made from pure PAN fibers. The other two samples, MF1 and MF2, are the magnetic composite fibers synthesized from stabilized PAN fibers after treatment with 0.3 M  $\text{Co}(\text{NO}_3)_2$  and 0.1 M  $\text{Fe}(\text{NO}_3)_3$ –0.2 M  $\text{Co}(\text{NO}_3)_2$ , respectively. The magnetic carbon nanocomposite fiber preparation process is illustrated in Scheme 1.

### 2.4 Characterization

Fourier transform infrared spectroscopy (FT-IR, Bruker Inc. Tensor 27) with hyperion 1000 ATR microscopy accessory was used to characterize the samples over the range of 4000 to  $500\text{ cm}^{-1}$  at a resolution of  $4\text{ cm}^{-1}$ .

The morphology of the samples was characterized with a scanning electron microscope (SEM, Hitachi S-3400) and a transmission electron microscope (TEM, FEI Tecnai G2 F20) with a field emission gun, operating at an accelerating voltage of 200 kV. The TEM samples were prepared by drying a drop of sample–ethanol suspension on carbon-coated copper TEM grids.

The thermal degradation behavior of the samples was studied with a thermo-gravimetric analysis (TGA Q-500, TA



Scheme 1 Schematic illustration of the fabrication of magnetic carbon composite fibers.

Instruments) from 25 to 750 °C in air atmosphere, with a flow rate of 60 mL min<sup>-1</sup> and a heating rate of 10 °C min<sup>-1</sup>.

The temperature dependent electrical resistivity (100–290 K) and magnetic field-dependent resistivity (290 K) measurements were carried out in a 9-T Physical Properties Measurement System (PPMS) by Quantum Design using a standard four-probe technique. Magnetic properties were also measured using the PPMS.

### 3. Results and discussion

#### 3.1 FT-IR analysis

Fig. 1 shows the FT-IR spectra of the electrospun PAN fibers, stabilized PAN fibers, carbonized PAN fibers and magnetic carbon nanocomposite fibers MF1/MF2. The peak at 2920 cm<sup>-1</sup> is due to the stretching vibration of the methylene group (-CH<sub>2</sub>-). The strong peak at 2240 cm<sup>-1</sup> corresponds to a characteristic absorption of the nitrile compound<sup>35,38</sup> and is assigned to the stretching vibration of the nitrile group (-CN-). The 1668 cm<sup>-1</sup> peak is due to the stretching vibration of carbon-carbon double bonds present at the end of the polymer chain.<sup>39,40</sup> The peaks at 1460 and 1360 cm<sup>-1</sup> are assigned to the bending vibrations of the methylene and methine group,<sup>31,41</sup> respectively. The evolution of the fiber composition during stabilization and carbonization is monitored by the FT-IR spectra, Fig. 1(b) and (c). The disappearance of the bands at 2240 (C≡N), 1453 and 2922 cm<sup>-1</sup> (aliphatic C-H) after stabilization confirms the reactions of dehydrogenation and dehydrocyanide. At the same time, several new peaks between 1200 and 1600 cm<sup>-1</sup> are observed, Fig. 1(b), indicating the formation of the C=C and C=N bands.<sup>42</sup> After annealing, the polymer fibers are converted into carbon fibers accompanied by the disappearance of the peaks in the typical range of 1000 to 1600 cm<sup>-1</sup>, Fig. 1(c). In MF1/MF2, a few intensive peaks between 500 and 700 cm<sup>-1</sup> (marked with the grey background and the inset in Fig. 1 shows an enlarged view) are observed corresponding to the metal-oxygen vibration modes of the metal oxide nanoparticles, Fig. 1(d) and (e). The specific composition of the nanoparticles was carefully investigated in the following sections.

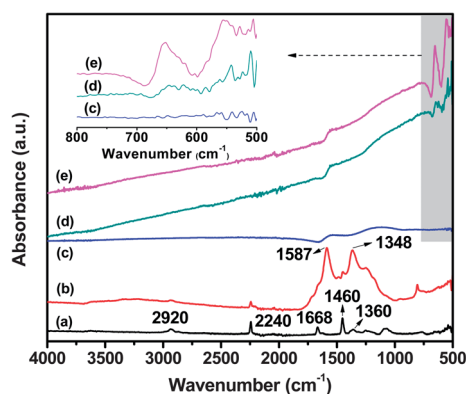


Fig. 1 (a) PAN, (b) stabilized PAN, (c) carbonized PAN, (d) MF1 and (e) MF2.

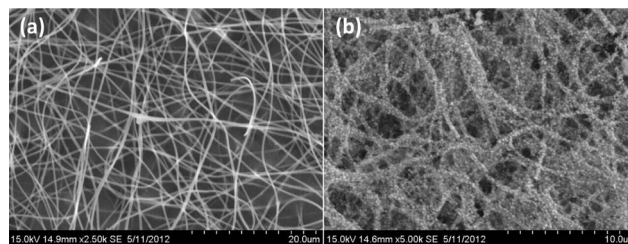


Fig. 2 SEM microstructure of (a) CF and (b) MF1.

#### 3.2 Microstructure characterization

To obtain uniform nano-sized PAN fibers, the electrospinning parameters are optimized following our previous report.<sup>35</sup> The applied voltage, volume feed rate and tip-to-collector distance are set at 20.0 kV, 20.0 μL min<sup>-1</sup> and 20.0 cm, respectively. Fig. 2(a) shows the as-spun PAN fiber morphology with uniform size distribution (diameter: ~300 nm) and a smooth fiber surface. The as-spun PAN fibers were then oxidized at 250 °C in air to convert the C-C and C≡N into C=C, C=N bonds, which is a necessary step for further carbonization with the aim to avoid melting or fusion of the fibers.<sup>35,43</sup> After oxidation, a significant color change from white to dark yellow was observed. The nanoparticle coating on the fiber surface is quite simple that a dipping method in an inorganic salt solution has been used as described in the experimental part. Fig. 2(b) shows the nanocomposite fibers doped with 0.3 M Co(NO<sub>3</sub>)<sub>2</sub>. The nanoparticles are fairly uniformly distributed on the carbonized fiber surface, which demonstrates the feasibility of this simple approach in forming a nanostructured coating on the 1D fiber surface. In addition, the diameter of the carbon fiber and the size of the nanoparticles can be tuned by the electrospinning process and the dip-coating/annealing process, respectively. These geometric modifications of nanocomposite fibers will definitely affect the electronic structure of the nanocomposite fibers and thus result in the change of their magnetic and magnetoresistive properties.

Fig. 3(a) shows the TEM image of MF1, depicting that the nanoparticles have grown on the fiber surface. It is worth mentioning that the fiber diameter is decreased to ~200 nm due to the fiber shrinkage during stabilization and carbonization.<sup>35,44</sup> The typical particle size is in the range of 50–200 nm (average: 100 nm). Energy-filtered TEM (EFTEM) is conducted on the sample to further clarify the specific component of the nanoparticle structure. The elemental maps of carbon, oxygen and cobalt are shown in Fig. 3(b)–(d). The EFTEM mapping provides a 2-dimensional elemental distribution. The brighter area in the elemental map indicates the higher concentration of the corresponding element in that area. They are shown in different colors, for the purpose of identifying their positions within the nanoparticles. Fig. 3(b) depicts the carbon map showing the dark nanoparticles decorated in the bright carbon fiber substrate. There are no shining spots on the nanoparticles indicating that the carbon element is not involved in the nanoparticle formation. The oxygen map, Fig. 3(c), shows light color distribution covering the whole nanocomposite

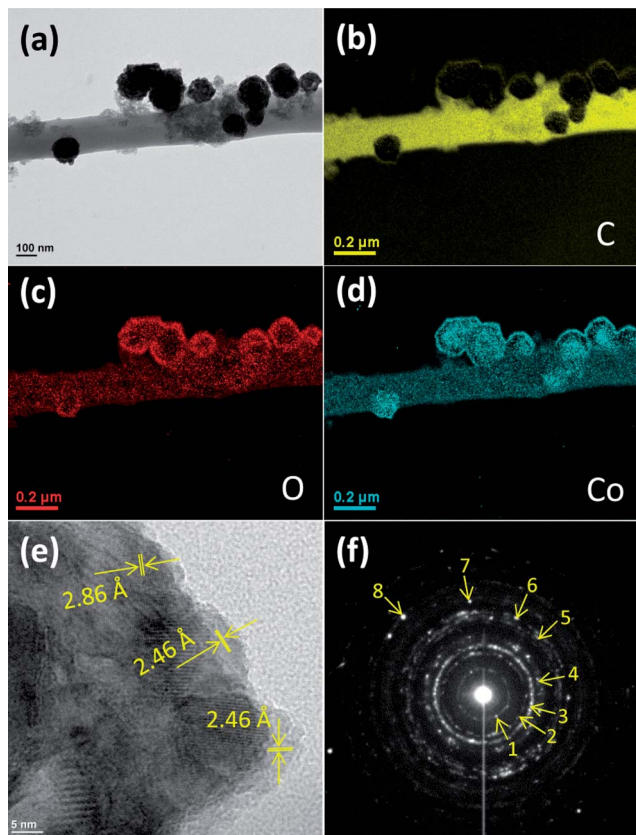


Fig. 3 (a) TEM of MF1, (b) C mapping, (c) O mapping, (d) Co mapping, (e) high resolution TEM and (f) SAED of MF1.

structure but intense circular color surrounding the nanoparticles, indicating that the core areas of nanoparticles have low O but the shell areas have high O. With regard to the Co mapping, Fig. 3(d), a similar color pattern was observed as that for oxygen that color distributes through the whole nanocomposites. The intense color in the core area of the nanoparticles indicates that Co is mainly distributed in the nanoparticle core. And the bright circles with narrow thickness reveal that the Co element is also distributed at the outside of the nanoparticles. The light color on the fiber surface may be attributed to the smaller cobalt nanoparticles with a particle size of 5–10 nm. These nanostructures were very easy to oxidized and thus a similar oxygen pattern was observed on the fiber surface. Together with the similar circle pattern observed in oxygen mapping, the inner core and outer shell of the nanoparticles were identified as pure cobalt and cobalt oxide, respectively. The core-shell structure formation mechanism is explained as follows. First, the cobalt nitrate hexahydrate underwent a dehydration process, giving cobalt nitrate monohydrate as an intermediate at 150 °C and then was further decomposed to  $\text{Co}_3\text{O}_4$  at 280 °C.<sup>45</sup> Secondly, the formed  $\text{Co}_3\text{O}_4$  was reduced to Co nanoparticles by the annealed carbon fiber at elevated temperature. Thirdly, the Co nanoparticles were slowly oxidized at the surface to form a solid  $\text{Co}_3\text{O}_4$  shell after exposure to air, preventing further oxidation of the cobalt core and thus forming the core-shell structure.

To identify the crystalline structure of the nanoparticles, HRTEM is carried out focusing on the edge area of a nanoparticle, Fig. 3(e). A measured lattice fringe of 2.46 Å corresponds to the (311) plane of  $\text{Co}_3\text{O}_4$ , while the lattice fringe of 2.86 Å corresponds to the (220) plane of  $\text{Co}_3\text{O}_4$  (PDF# 42-1467). The selected area electron diffraction (SAED) patterns, Fig. 3(f), show the crystalline planes of the  $\text{Co}_3\text{O}_4$  shell 1(111), 2(220), 3(311), 4(400), 5(422), 6(511) (PDF# 42-1467) and the Co core 7(110) and 8(201) (PDF# 05-0727), which are consistent with the HRTEM and EFTEM observations.

This “dip-coating” method has been demonstrated as a general approach that can be utilized to coat binary metal oxide (BMO) nanoparticles by replacing the  $\text{Co}(\text{NO}_3)_2$  solution with the  $\text{Fe}(\text{NO}_3)_2$ - $\text{Co}(\text{NO}_3)_2$  mixture. Fig. 4(a) shows the nanocomposite fibers that were coated by BMO nanoparticles (MF2). Different from MF1 with a significant number of nanoparticles attached on the fiber surface, the nanoparticle distribution density is obviously lower in MF2 probably due to the fact that the nanoparticles have been partially embedded in the fiber structure. Fig. 4(b) shows the TEM image of MF2. The dark dots within the gray fiber substrate represent the uniformly distributed nanoparticles. Taking a closer look at the end of the fiber, nanoparticles are observed both on the fiber surface (small amount) and in the main fiber body (majority).

To confirm the BMO composition and crystalline structure, EFTEM and HRTEM were conducted on MF2, Fig. 5. Carbon, oxygen, iron and cobalt elements were mapped with different colors, as shown in Fig. 5(a)–(d), respectively. The carbon map shows the bright color of the fiber substrate with black dots within the body and a dent on the right top-end, indicating that carbon did not involve in the BMO nanoparticle formation. Similar features were observed in the elemental mapping of oxygen, iron and cobalt that the color distribution is very uniform throughout the MF2, and a convex part appears at the exact position of the dent in the carbon mapping. These results reveal that the BMO nanoparticles are evenly dispersed within the carbon fiber and thus iron, cobalt and oxygen exhibit the same elemental mapping pattern. The HRTEM image in Fig. 5(e) shows the core-shell structure of the surface decorated BMO nanoparticle. The measured shell lattice fringe of 2.74 Å was attributed to the (002) plane of  $\text{Co}_2\text{O}_3$  (PDF# 02-0770). From the core area, two lattice fringes measured to be 2.47 Å and 2.17 Å are identified as  $\text{Co}_2\text{O}_3$  (102, PDF# 02-0770) and FeO (200, PDF# 06-0615), respectively. The SAED patterns, Fig. 5(f),

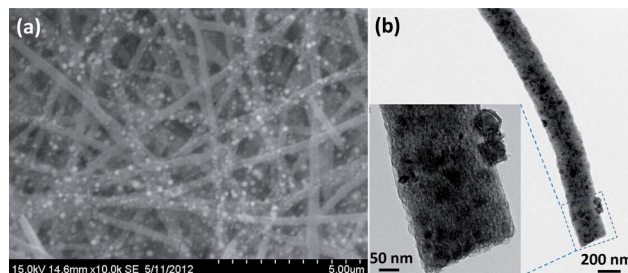


Fig. 4 (a) SEM of MF2, (b) TEM of MF2. The inset shows the enlarged area of the MF2.

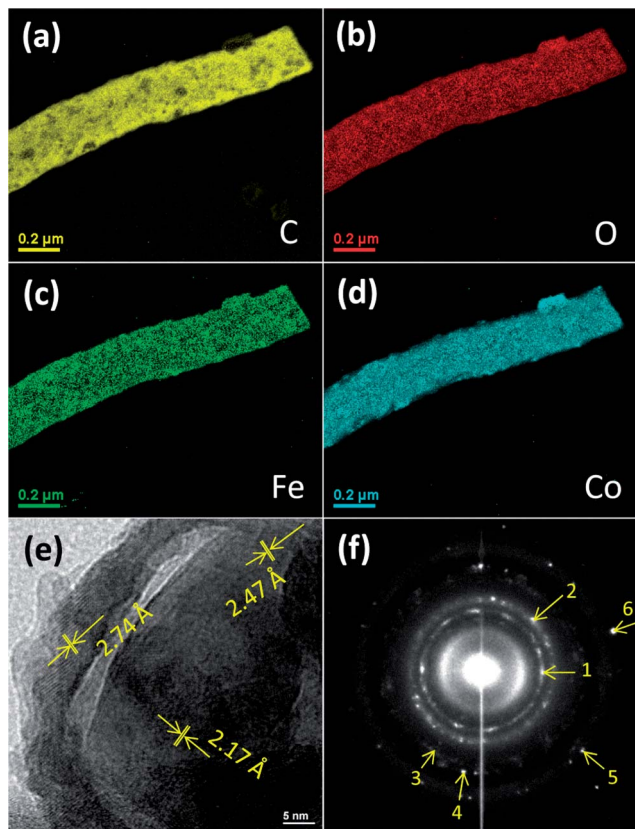


Fig. 5 Elemental mapping of MF2 (a) C mapping, (b) O mapping, (c) Fe mapping, (d) Co mapping, (e) high resolution TEM of MF2, and (f) SAED of MF2 and its corresponding crystal planes 1(102), 2(200), 3(220), 4(311), 5(222) and 6(400).

show the crystalline planes of the  $\text{Co}_2\text{O}_3$  1(102, PDF# 02-0770), and FeO 2(200), 3(220), 4(311), 5(222) and 6(400) (PDF# 06-0615). All these results confirm the  $\text{Co}_2\text{O}_3$  and FeO binary metal oxide structure, which are consistent with the HRTEM and EFTEM observations.

### 3.3 Electrical conductivity

Fig. 6(a) shows the variation of resistivity as a function of temperature for CF, MF1 and MF2. It is observed that the

resistivity of CF decreases continuously with increasing temperature, indicating an obvious semiconducting behavior from 100 to 290 K.<sup>8,46,47</sup> The curves for MF1 and MF2 are more likely flattened, showing metal-like conduction behavior within the wide temperature range. Moreover, it is interesting to observe that CF and MF1 meet a cross point at 230 K. MF1 exhibits smaller resistivity than that of CF below this point, while it exceeds the resistivity of CF above 230 K. The comparable resistivity of MF1 with CF is attributed to the non-continuous nanostructures that hardly create electron transportation pathways between decorated particles. While MF2 shows significantly lower resistance compared to CF and MF1 due to the continuous feature of the nanostructures embedded in the carbon fiber as evidenced by the TEM observations in Fig. 4(b). The embedded nanoparticles would serve as catalysts facilitating graphitized carbon formation surrounding the nanoparticles.<sup>48</sup> This graphitized carbon exhibits higher conductivity as compared to the amorphous carbon. Therefore, lower resistivity is observed in MF2. Rescaling the resistance curves of MF1 and MF2 in Fig. 6(b), it is interesting to find that both curves show unique temperature dependent resistance features. The MF1 exhibits a negative temperature coefficient initially and then switches to a positive temperature coefficient starting at a temperature of  $\sim 230$  K. This positive temperature coefficient of resistance is a signature of metallic conduction, in contrast to the negative temperature coefficient and thermally activated behavior as observed in the pellets of iron oxide nanoparticles.<sup>49,50</sup> While MF2 shows a similar negative temperature coefficient up to 240 K and thereafter the resistance is nearly independent of the temperature within the range of 240–290 K.

### 3.4 Magnetic property

Fig. 7 shows the room temperature magnetic hysteresis loops of MF1 and MF2. In a previous study, the magnetic property of CF has been studied extensively. Typically, the polyacrylonitrile based CF shows diamagnetic properties and a very small negative susceptibility on the order of  $10^{-6}$  emu  $\text{g}^{-1}$ .<sup>51</sup> Compared to the large magnetization of the nanocomposite fibers (15–20 emu  $\text{g}^{-1}$ ), the magnetization of the CF can be ignored. Both MF1 and MF2 reach saturation magnetization

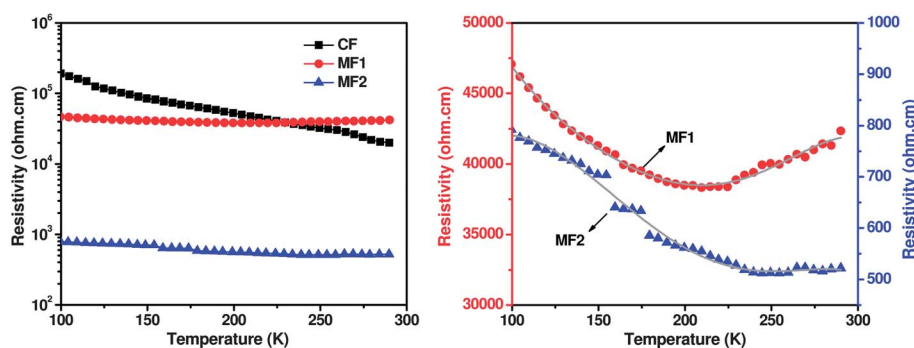


Fig. 6 (a) Zero field temperature dependent resistivity of CF, MF1 and MF2 and (b) temperature dependent resistivity of MF1 and MF2 with a narrowed scale range, the gray curves represent smooth fitting of the experimental data.

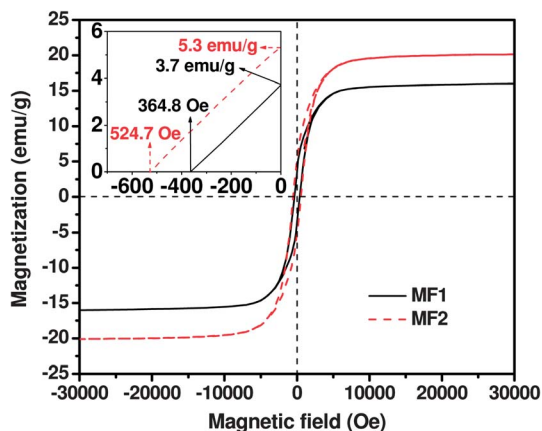


Fig. 7 Magnetic hysteresis loops of MF1 and MF2 at room temperature.

( $M_s$ ) at a field of 30 000 Oe, where the increase of the magnetic field cannot increase the magnetization further. The actual weight fractions of the magnetic nanostructure part and the non-magnetic carbon fiber were determined by using thermogravimetric analysis (TGA). Fig. 8 shows the thermal degradation profiles of MF1 and MF2 in air atmosphere. The sharp weight loss between 300 and 420 °C indicates the burning of carbon nanofibers, leaving behind metal oxides. The MF1 curve shows a slight increase after 420 °C due to the oxidation of the cobalt core. The weight fraction of the solid residue is determined at 700 °C, where carbon has been completely burned out. The weight fraction of the magnetic nanostructure in MF1 and MF2 is 69.7 and 45.6%, respectively. As seen in Fig. 7, MF2 shows a relatively larger  $M_s$  of 20.1  $\text{emu g}^{-1}$  than that of MF1 (16.0  $\text{emu g}^{-1}$ ). Excluding the weight fraction of the carbon nanofiber, the magnetic nanostructure in MF2 shows a much larger  $M_s$  ( $20.1/45.6\% = 44.1 \text{ emu g}^{-1}$ ) than that of the magnetic part in MF1 ( $16.0/69.7\% = 23.0 \text{ emu g}^{-1}$ ) due to the higher magnetic moment of the doped iron (218.0  $\text{emu g}^{-1}$ ) than cobalt (161.0  $\text{emu g}^{-1}$ ). The coercivity ( $H_c$ , Oe) indicates the external applied magnetic field necessary to return the material to a zero magnetization condition, and the remnant magnetization ( $M_r$ ) is the residue magnetization after the applied field is

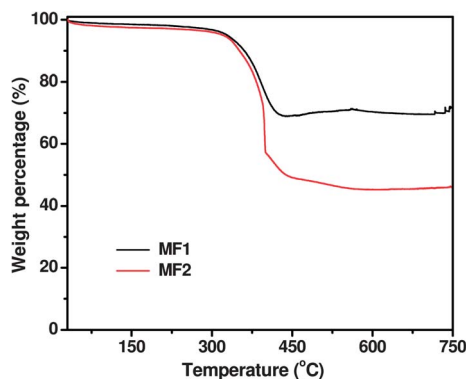


Fig. 8 TGA profiles of MF1 and MF2 in air with a heating rate of 10 °C  $\text{min}^{-1}$ .

reduced to zero. Both values can be read from the axis crossing points, inset of Fig. 7. MF2 shows relatively higher  $H_c = 524.7$  Oe and  $M_r = 5.3 \text{ emu g}^{-1}$  as compared to MF1 which exhibits  $H_c$  and  $M_r$  at 364.8 Oe and 3.7  $\text{emu g}^{-1}$ , respectively. Both  $H_c$  values are significantly larger than 200 Oe, indicating their hard ferromagnetic behaviors.

### 3.5 Magnetoresistance (MR)

Fig. 9 shows the magnetoresistance of CF and nanocomposite fibers at 290 K. The MR results demonstrate different magnetic field dependent behaviors that can be divided into two groups, one is positive MR obtained from CF and MF2, the other is very large negative MR from MF1. This unique phenomenon reveals that the electrical conductivity of the 1D fiber can be tuned *via* this facile nanostructure coating process. Positive MR observed in CF and MF2 was attributed to the shrinkage in the overlap of the electron wave functions after applying a magnetic field and thus the reduced average hopping length.<sup>52</sup> Similar phenomena have been reported in a variety of materials including carbon nanostructures,<sup>3,53</sup> metal oxides,<sup>54,55</sup> conductive polymers<sup>56</sup> and composites.<sup>8,13,46</sup> However, the MR of MF1 is negative with significantly larger magnitude. To reveal the physical mechanism, a few models have been proposed to explain the negative MR phenomena related to the conduction mechanism. For example, strong localization in the highly disordered materials<sup>57,58</sup> made the conduction mechanism follow a variable range hopping (VRH) model, which has been realized as the major reason for obtaining negative MR. The VRH model is given by eqn (1)

$$\sigma = \sigma_0 \exp \left[ - \left( \frac{T_0}{T} \right)^{1/n} \right] \quad (1)$$

where  $T_0$  is the characteristic Mott temperature related to the electronic wave function localization degree and  $\sigma_0$  is a constant representing the conductivity at infinite low temperature limit. The value of  $n$  assumes 4, 3, and 2 for three-, two-, and one-dimensional systems, respectively. Besides, the quantum interference effect, which involves quantum particles exhibiting both wave-like and particle-like properties, also plays a key role in negative MR. Sivan *et al.*<sup>59</sup> have evaluated a quantum

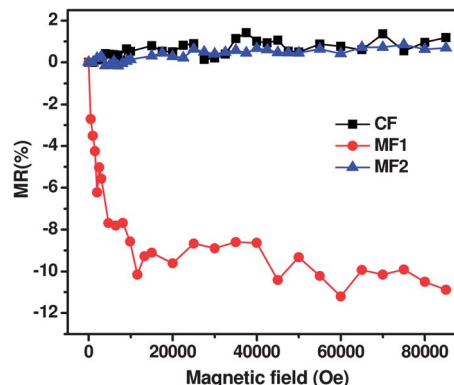


Fig. 9 The magnetoresistance of CF, MF1 and MF2.

interference effect on VRH, and found that the modification of the quantum interference between many possible hopping paths in the magnetic field would lead to a negative MR ( $MR \propto -H^x T^{-y}$ , where  $x = 1$  or  $2$ ,  $y = 3/(1 + d)$  and  $d$  is the effective dimensionality of the hopping conduction). Unfortunately, both MR and conductivity fitting results reveal that (1) the MR of MF1 is not directly related to any forms of  $-H^x T^{-y}$  and (2) the conduction mechanism of MF1 (fitting data from Fig. 6 by eqn (1)) is inconsistent with VRH mode. Due to the unique core-shell structure of the decorated nanoparticles and their strong interfacial interaction with carbon fibers in MF1, the negative MR is probably caused by spin-dependent scattering, similar to those observed in magnetic granular solids.<sup>60,61</sup> The cobalt core serves as a magnetic scattering center. In zero magnetic field, the orientation of the magnetization of each cobalt core is random, resulting in a spin-disordered state. The applied magnetic field aligns all the cobalt core moments and reduces the spin disorder, which reduces the spin dependent scattering and leads to a reduced resistance, thus resulting in a negative MR. The unique MR switching phenomena observed in these nanocomposite fibers offer a promising approach to achieve the desired MR property. However, to control the switching phenomena, further studies need to be done to achieve an atomic level control of nanocomposites and then tune their electronic structure and magnetic properties effectively.

## 4. Conclusions

A facile approach to obtain magnetic carbon nanocomposite fibers with metal oxide nanoparticles decorated on the fibers has been demonstrated. Electrospun polyacrylonitrile nanofibers were stabilized at elevated temperature in air to convert their hydrophobic surface<sup>62</sup> to hydrophilic and then they were used as templates to load inorganic metal precursors in a water based solution. The magnetic carbon nanocomposite fibers were manufactured from the metal doped polymer nanofibers via an annealing process, where polymer nanofibers were converted into carbon nanofibers and the metal ions were transformed into metal oxide nanoparticles simultaneously. By loading a single cobalt nitrate precursor, the obtained Co@Co<sub>3</sub>O<sub>4</sub> nanoparticles are mainly adhered on the fiber surface. The Co@Co<sub>3</sub>O<sub>4</sub> nanoparticles were formed after thermal decomposition, reduction and oxidation processes. While using a cobalt nitrate-iron nitrate mixture, the nanoparticles were mainly embedded within the nanofiber body. Due to different structures and compositions of the MF1/MF2 nanocomposites, unique temperature dependent resistance behavior was observed where MF1 shows both positive and negative temperature coefficients within the temperature range of 100–290 K. Moreover, large negative and positive magnetoresistance were observed in MF1 and MF2, respectively. This synthetic method is general, which is readily used in the fabrication of other fibrous nanocomposites by replacing the metal precursors. The unique electric properties of these novel nanostructures offer them a promising future in various potential applications including electronic devices,<sup>63</sup> catalysts,<sup>64</sup> electrochemical supercapacitors/batteries,<sup>65,66</sup> etc.

## Acknowledgements

This work is supported by the National Science Foundation – Nanomanufacturing (CMMI 13-14486). The support from NSF Materials Processing and Manufacturing (CMMI 10-30755) to purchase DSC and TGA is kindly acknowledged. D.P.Y. acknowledges the support from the NSF under Grant no. DMR 13-06392.

## References

- 1 M. N. Baibich, J. M. Broto, A. Fert, F. N. Van Dau, F. Petroff, P. Etienne, G. Creuzet, A. Friederich and J. Chazelas, *Phys. Rev. Lett.*, 1988, **61**, 2472.
- 2 S. Krompiewski, R. Gutiérrez and G. Cuniberti, *Phys. Rev. B: Condens. Matter*, 2004, **69**, 155423.
- 3 J. Zhu, S. Wei, N. Haldolaarachchige, J. He, D. P. Young and Z. Guo, *Nanoscale*, 2012, **4**, 152–156.
- 4 F. Muñoz-Rojas, J. Fernández-Rossier and J. J. Palacios, *Phys. Rev. Lett.*, 2009, **102**, 136810.
- 5 J. Zhu, M. Chen, Q. He, L. Shao, S. Wei and Z. Guo, *RSC Adv.*, 2013, **3**, 22790–22824.
- 6 Ö. Mermer, G. Veeraraghavan, T. L. Francis, Y. Sheng, D. T. Nguyen, M. Wohlgenannt, A. Köhler, M. K. Al-Suti and M. S. Khan, *Phys. Rev. B: Condens. Matter*, 2005, **72**, 205202.
- 7 T. L. Francis, Ö. Mermer, G. Veeraraghavan and M. Wohlgenannt, *New J. Phys.*, 2004, **6**, 185.
- 8 J. Zhu, H. Gu, Z. Luo, N. Haldolaarachchige, D. P. Young, S. Wei and Z. Guo, *Langmuir*, 2012, **28**, 10246–10255.
- 9 H. Gu, Y. Huang, X. Zhang, Q. Wang, J. Zhu, L. Shao, N. Haldolaarachchige, D. P. Young, S. Wei and Z. Guo, *Polymer*, 2012, **53**, 801–809.
- 10 J. Guo, H. Gu, H. Wei, Q. Zhang, N. Haldolaarachchige, Y. Li, D. P. Young, S. Wei and Z. Guo, *J. Phys. Chem. C*, 2013, **117**, 10191–10202.
- 11 H. Gu, J. Guo, X. Zhang, Q. He, Y. Huang, H. A. Colorado, N. Haldolaarachchige, H. Xin, D. P. Young, S. Wei and Z. Guo, *J. Phys. Chem. C*, 2013, **117**, 6426–6436.
- 12 X. Zhang, S. Wei, N. Haldolaarachchige, H. A. Colorado, Z. Luo, D. P. Young and Z. Guo, *J. Phys. Chem. C*, 2012, **116**, 15731–15740.
- 13 J. Zhu, Z. Luo, S. Wu, N. Haldolaarachchige, D. P. Young, S. Wei and Z. Guo, *J. Mater. Chem.*, 2012, **22**, 835–844.
- 14 Z. Guo, S. Park, H. T. Hahn, S. Wei, M. Moldovan, A. B. Karki and D. P. Young, *Appl. Phys. Lett.*, 2007, **90**, 053111.
- 15 M. Fujii, M. Matsui, S. Motojima and Y. Hishikawa, *Thin Solid Films*, 2002, **409**, 78–81.
- 16 H. Gu, X. Zhang, H. Wei, Y. Huang, S. Wei and Z. Guo, *Chem. Soc. Rev.*, 2013, **42**, 5907–5943.
- 17 E. S. Steigerwalt, G. A. Deluga and C. M. Lukehart, *J. Phys. Chem. B*, 2002, **106**, 760–766.
- 18 M.-C. Wu, A. Sapi, A. Avila, M. Szabo, J. Hiltunen, M. Huuhtanen, G. Toth, A. Kukovec, Z. Konya, R. Keiski, W.-F. Su, H. Jantunen and K. Kordas, *Nano Res.*, 2011, **4**, 360–369.

- 19 V. Thavasi, G. Singh and S. Ramakrishna, *Energy Environ. Sci.*, 2008, **1**, 205–221.
- 20 C. Kim, B. T. N. Ngoc, K. S. Yang, M. Kojima, Y. A. Kim, Y. J. Kim, M. Endo and S. C. Yang, *Adv. Mater.*, 2007, **19**, 2341–2346.
- 21 J. S. Im, S.-J. Park and Y.-S. Lee, *Mater. Res. Bull.*, 2009, **44**, 1871–1878.
- 22 Y. Zhang, X. He, J. Li, Z. Miao and F. Huang, *Sens. Actuators, B*, 2008, **132**, 67.
- 23 J. Yoon, S. K. Chae and J.-M. Kim, *J. Am. Chem. Soc.*, 2007, **129**, 3038–3039.
- 24 X. Wang, C. Drew, S.-H. Lee, K. J. Senecal, J. Kumar and L. A. Samuelson, *Nano Lett.*, 2002, **2**, 1273–1275.
- 25 K. Sawicka, P. Gouma and S. Simon, *Sens. Actuators, B*, 2005, **108**, 585–588.
- 26 X. Wang, Y.-G. Kim, C. Drew, B.-C. Ku, J. Kumar and L. A. Samuelson, *Nano Lett.*, 2004, **4**, 331–334.
- 27 M. A. Perez, M. D. Swan and J. W. Louks, *US Pat.* 6, 2000, 110, 588.
- 28 W. Daan and S. S. Ulrich, *Angew. Chem., Int. Ed.*, 2004, **43**, 2480–2495.
- 29 C. F. J. Faul and M. Antonietti, *Adv. Mater.*, 2003, **15**, 673–683.
- 30 G. M. Whitesides and M. Boncheva, *Proc. Natl. Acad. Sci. U. S. A.*, 2002, **99**, 4769–4774.
- 31 D. Zhang, A. B. Karki, D. Rutman, D. P. Young, A. Wang, D. Cocke, T. H. Ho and Z. Guo, *Polymer*, 2009, **50**, 4189–4198.
- 32 M. Chen, H. Qu, J. Zhu, Z. Luo, A. Khasanov, A. S. Kucknoor, N. Haldolaarachchige, D. P. Young, S. Wei and Z. Guo, *Polymer*, 2012, **53**, 4501.
- 33 J. Zhu, S. Wei, R. Patil, D. Rutman, A. S. Kucknoor, A. Wang and Z. Guo, *Polymer*, 2011, **52**, 1954–1962.
- 34 S. Wei, J. Sampathi, Z. Guo, N. Anumandla, D. Rutman, A. Kucknoor, L. James and A. Wang, *Polymer*, 2011, **52**, 5817–5829.
- 35 J. Zhu, S. Wei, D. Rutman, N. Haldolaarachchige, D. P. Young and Z. Guo, *Polymer*, 2011, **52**, 2947–2955.
- 36 J. Zhu, S. Wei, X. Chen, A. B. Karki, D. Rutman, D. P. Young and Z. Guo, *J. Phys. Chem. C*, 2010, **114**, 8844–8850.
- 37 X. Chen, S. Wei, C. Gunesoglu, J. Zhu, C. S. Southworth, L. Sun, A. B. Karki, D. P. Young and Z. Guo, *Macromol. Chem. Phys.*, 2010, **211**, 1775–1783.
- 38 *Spectrometric Identification of Organic Compounds*, ed. R. M. Silverstein, F. X. Webster and D. Kiemle, John Wiley and Sons, Inc., Hoboken, 2005.
- 39 P. De, D. N. Sathyanarayana, P. Sadasivamurthy and S. Sridhar, *Eur. Polym. J.*, 2002, **38**, 847–855.
- 40 P. De, D. N. Sathyanarayana, P. Sadasivamurthy and S. Sridhar, *Polymer*, 2001, **42**, 8587–8593.
- 41 R. B. Mathur, O. P. Bahl and P. Sivram, *Curr. Sci.*, 1992, **62**, 662–669.
- 42 T. Usami, T. Itoh, H. Ohtani and S. Tsuge, *Macromolecules*, 1990, **23**, 2460–2465.
- 43 S. Moon and R. J. Farris, *Carbon*, 2009, **47**, 2829–2839.
- 44 I. Mochida, S. H. Yoon, N. Takano, F. Fortin, Y. Korai and K. Yokogawa, *Carbon*, 1996, **34**, 941–956.
- 45 S. A. A. Mansour, *Mater. Chem. Phys.*, 1994, **36**, 317–323.
- 46 J. Zhu, X. Zhang, N. Haldolaarachchige, Q. Wang, Z. Luo, J. Ryu, D. P. Young, S. Wei and Z. Guo, *J. Mater. Chem.*, 2012, **22**, 4996–5005.
- 47 S. Chakrabarti, D. Banerjee and R. Bhattacharyya, *J. Phys. Chem. B*, 2002, **106**, 3061–3064.
- 48 J. Zhu, S. Pallavkar, M. Chen, N. Yerra, Z. Luo, H. A. Colorado, H. Lin, N. Haldolaarachchige, A. Khasanov, T. C. Ho, D. P. Young, S. Wei and Z. Guo, *Chem. Commun.*, 2013, **49**, 258–260.
- 49 K. Liu, L. Zhao, P. Klavins, F. E. Osterloh and H. Hiramatsu, *J. Appl. Phys.*, 2003, **93**, 7951.
- 50 L. Savini, E. Bonetti, L. Del Bianco, L. Pasquini, L. Signorini, M. Coisson and V. Selvaggini, *J. Magn. Magn. Mater.*, 2003, **262**, 56–59.
- 51 K. Kaneko, K. Yamaguchi, C. Ishii, S. Ozeki, S. Hagiwara and T. Suzuki, *Chem. Phys. Lett.*, 1991, **176**, 75–78.
- 52 *Handbook of Conducting Polymers*, ed. T. A. Skotheim, R. L. Elsenbaumer and J. R. Reynolds, New York, Marcel Dekker, 1998.
- 53 A. Y. Kasumov, I. I. Khodos, P. M. Ajayan and C. Colliex, *Europhys. Lett.*, 1996, **34**, 429–434.
- 54 Y. Matsumoto, M. Murakami, T. Shono, T. Hasegawa, T. Fukumura, M. Kawasaki, P. Ahmet, T. Chikyow, S.-y. Koshihara and H. Koinuma, *Science*, 2001, **291**, 854–856.
- 55 T. Motohashi, R. Ueda, E. Naujalis, T. Tojo, I. Terasaki, T. Atake, M. Karppinen and H. Yamauchi, *Phys. Rev. B: Condens. Matter*, 2003, **67**, 064406.
- 56 Y. Long, L. Zhang, Z. Chen, K. Huang, Y. Yang, H. Xiao, M. Wan, A. Jin and C. Gu, *Phys. Rev. B: Condens. Matter*, 2005, **71**, 165412.
- 57 Y. Wang and J. J. Santiago-Avilés, *Appl. Phys. Lett.*, 2006, **89**, 123119.
- 58 A. A. Bright, *Carbon*, 1979, **17**, 259–263.
- 59 U. Sivan, O. Entin-Wohlman and Y. Imry, *Phys. Rev. Lett.*, 1988, **60**, 1566–1569.
- 60 J. Q. Xiao, J. S. Jiang and C. L. Chien, *Phys. Rev. Lett.*, 1992, **68**, 3749–3752.
- 61 S.-J. Cho, S. M. Kauzlarich, J. Olamit, K. Liu, F. Grandjean, L. Rebbouh and G. J. Long, *J. Appl. Phys.*, 2004, **95**, 6804.
- 62 L. Feng, S. Li, H. Li, J. Zhai, Y. Song, L. Jiang and D. Zhu, *Angew. Chem., Int. Ed.*, 2002, **41**, 1221–1223.
- 63 S. K. Chae, H. Park, J. Yoon, C. H. Lee, D. J. Ahn and J. M. Kim, *Adv. Mater.*, 2007, **19**, 521–524.
- 64 T. He, Z. Zhou, W. Xu, F. Ren, H. Ma and J. Wang, *Polymer*, 2009, **50**, 3031.
- 65 Q. Cheng, J. Tang, J. Ma, H. Zhang, N. Shinya and L.-C. Qin, *J. Phys. Chem. C*, 2011, **115**, 23584–23590.
- 66 M.-H. Ryu, K.-N. Jung, K.-H. Shin, K.-S. Han and S. Yoon, *J. Phys. Chem. C*, 2013, **117**, 8092–8098.